Neoclassical simulation of tokamak plasmas using the continuum gyrokinetic code TEMPEST

X. Q. Xu
Lawrence Livermore National Laboratory, Livermore, California 94550, USA
(Received 7 December 2007; published 29 July 2008; publisher error corrected 31 July 2008)

We present gyrokinetic neoclassical simulations of tokamak plasmas with a self-consistent electric field using a fully nonlinear (full-f) continuum code TEMPEST in a circular geometry. A set of gyrokinetic equations are discretized on a five-dimensional computational grid in phase space. The present implementation is a method of lines approach where the phase-space derivatives are discretized with finite differences, and implicit backward differencing formulas are used to advance the system in time. The fully nonlinear Boltzmann model is used for electrons. The neoclassical electric field is obtained by solving the gyrokinetic Poisson equation with self-consistent poloidal variation. With a four-dimensional $(\psi, \theta, \epsilon, \mu)$ version of the TEMPEST code, we compute the radial particle and heat fluxes, the geodesic-acoustic mode, and the development of the neoclassical electric field, which we compare with neoclassical theory using a Lorentz collision model. The present work provides a numerical scheme for self-consistently studying important dynamical aspects of neoclassical transport and electric field in toroidal magnetic fusion devices.

DOI: 10.1103/PhysRevE.78.016406 PACS number(s): 52.65.Tt, 52.25.Fi, 52.35.Ra, 52.55.Fa

I. INTRODUCTION

An outstanding scientific problem in the plasma boundary lies in understanding the structure of the edge transport barrier, which forms spontaneously in high-performance (H-mode) discharges in tokamaks. At present, the physics governing the structure of the edge pedestal remains controversial because of the wide range of physical processes, scale lengths, and time scales that come into play. First, the fact that the fundamental character of the medium changes from a collisional fluid plasma to a collisionless Vlasov plasma as one moves inward across the pedestal forces one to go beyond the theoretical descriptions of plasma transport presently used in simulations. Second, the radial width of the pedestal observed in experiment is comparable to the radial width of individual particle orbits (leading to large distortions of the local distribution function from a Maxwellian). Third the mean free path is long compared to the connection length in the hot plasma at the top of the edge pedestal (violating the assumptions underlying a collisional fluid model). In contrast to several gyrokinetic code developments using the particle-in-cell (PIC) technique [1,2] in the pedestal region, we adopt the continuum method for our fully nonlinear (full-f) code development for the following reasons: (1) To avoid the intrinsic noise issue associated with a finite number of particles. When simulating equilibrium and fluctuations at the same time, the concern over noise is even more serious for fully nonlinear particle code development because the equilibrium particle noise in full-f simulations could become the order of the turbulent fluctuation due to $\langle |e\phi_{\rm noise}/T|^2 \rangle \propto 1/N_{\rm cell}$ [3,4]. Here $N_{\rm cell}$ is the number of particles in one grid cell. In fusion edge plasma simulations it has been estimated that a large number of particles (on the order of 1000) per grid cell is required to reduce the particle noise level down to the experimentally measured turbulence intensity $\langle |e\phi_{\rm expt}/T|^2 \rangle \simeq 10^{-4}$ for high confinement mode [5]. (2) To utilize existing Fokker-Planck collision packages developed in the community over the years by solving the nonlinear Fokker-Planck collision operator on velocity meshes.

In a magnetized plasma with straight field lines, the particle orbits are circular gyrations, and classical diffusion refers to the transport of particles due to Coulomb collisions, taking the particle gyro-orbits in the magnetic field into account. In a toroidal magnetic field, a single particle primarily undergoes parallel streaming along the magnetic field line and drifts across the field. The combination of the two motions produces various particle orbits when projecting its three-dimensional orbit onto a poloidal cross section. The orbits of passing particles are closed curves which do not quite coincide with flux surfaces because of the drift motion across the magnetic field. The banana orbits of trapped particles are traced by bounce motion along the field lines, accompanied by a slow drift motion across the magnetic field with the shape of a banana. Trapped particles are confined inside a magnetic well, typically outboard of the torus. Neoclassical transport refers to the random scattering of particle orbits by Coulomb collisions. The particle radial displacement in one collision time is typically enhanced, because the displacement of the gyrocenter from the original magnetic surface is generally larger than the gyroradius. Neoclassical turbulent transport refers to the random scattering of particle orbits due to small-scale turbulent decorrelation. Therefore, the success of neoclassical simulations relies on the accurate numerical description of the passing and trapped particle orbits, Coulomb collisions and turbulence.

In neoclassical plasmas, a radial electric field arises because of the different diffusion rates of ions and electrons. This electric field ensures quasineutrality and makes the radial fluxes of electrons and ions equal. This flux corresponds to the flux arising from ion-electron collisions. So far, either in particle simulations or continuum simulations, the electrostatic potential is typically assumed to be constant on a flux surface [1,2,6]. The radial electric field development is evaluated according to the radial Ampére-Maxwell law averaged over a closed-flux surface $4\pi\langle \mathbf{J}\cdot\nabla\psi\rangle + \partial\langle \mathbf{E}\cdot\nabla\psi\rangle/\partial t = 0$ (see the Appendix) where ψ is the poloidal magnetic flux, $\langle\cdots\rangle$ represents the flux surface average, and $\mathbf{J}$ is the sum of all the current in the plasma, including the classical polarization current, gyroviscosity current, and the ion guiding-

center current due to its orbital dynamics (the electron current is typically neglected in tokamak geometry, because it is smaller than the ion current by a factor of the mass ratio m_e/m_i). The steady-state neoclassical radial electric field E_ψ on a magnetic surface is obtained from the condition $\langle j_\psi \rangle = 0$. However, this method is incomplete in the sense that the poloidal electric field cannot be solved simultaneously in a consistent way. This is an unsatisfactory situation since the potential varies significantly in the edge plasma around the X point and in the divertor leg region due to contact with divertor plates. The gyrokinetic Poisson equation is seldom used because the small coefficient in front of the Poisson operator associated with the gyroradius makes the equation nearly singular when $\rho_i/L_p \ll 1$. Here, L_p is a characteristic gradient scale length of the plasma profile. For this reason, no single code exists to simulate both neoclassical transport and turbulence. However, there are efforts being undertaken to try to solve this dilemma [7,8]. In this paper, we develop a method to efficiently solve the gyrokinetic Poisson equation to remove the singularity and to correctly yield the neoclassical radial electric field.

Also in this paper, we report our present study of neoclassical transport with a self-consistent electric field using full-f continuum techniques. Because the problem is high dimensional with complicated particle orbits in phase space, it is not a trivial task to construct good difference schemes and choose a good set of coordinates. For example, when the particle energy and magnetic moment are used as the velocity coordinates, there are difficulties at the internal boundaries on the $v_\parallel = 0$ surface in phase space, such as the turning points for the trapped particles in real space, and cut cells on the $v_\parallel = 0$ boundary surface when two sheets of the distribution function (f^+ for $v_\parallel \geq 0$ and f^- for $v_\parallel < 0$) meet. The cut cells are generated by the boundary $v_\parallel^2 = (2/M_\alpha)(E_0 - \mu B - q\Phi_0) = 0$ line in velocity space (E_0, μ) for a given spatial location, which cuts through the background grid and results in irregular cut cells at the boundary. A full-f neoclassical simulation involves several types of physics interacting over several scales in time and space: Ion orbital dynamics is on the fast time scale [$\sim \omega_b (= v_{Ti}/qR_0)$ or ν_{ii}], and small spatial scale length $\rho_{i\theta}$; while the transport is on the slow time scale $\sim q^2 \nu_{ii} \rho_i^2 / L_{Ti}^2$ for the evolution of ion temperature, and operates over the large spatial scale $\sim L_{Ti}$. The time necessary to establish a rotational steady state is even longer, of order $\epsilon^{-3/2}$ times the neoclassical thermal equilibration times. Here ρ_i is the ion gyroradius, $\rho_{\theta,i}$ is the ion gyroradius at the poloidal magnetic field, ν_{ii} is the ion-ion collision rate, q is the safety factor, ϵ is the inverse aspect ratio, L_{Ti} is a characteristic gradient scale length of ion temperature, and $\rho_i \ll L_{Ti}$. We employ an implicit iteration method to solve the multiscale physics phenomena. The paper is organized as follows: Gyrokinetic equations are given in Sec. II, numerical schemes are presented in Sec. III, Sec. IV describes simulation results, and a summary is given in Sec. V.

II. GYROKINETIC EQUATIONS

Nonlinear gyrokinetic formalism focuses on low-frequency electromagnetic fluctuations that are observed in inhomogeneous magnetic plasmas [9,10]. It has been proven to be a useful theoretical foundation for analytical nonlinear kinetic models, gyrokinetic PIC and continuum simulations [11]. In TEMPEST, evolution of the plasma species is determined by coupled ion and electron kinetic equations for the time-dependent five-dimensional (5D) distribution functions simplified from Qin *et al.* [12] and Hahm [13], which is described in Ref. [14]. We present them here again for the sake of completeness. The gyrocenter distribution function $F_\alpha(\bar{\mathbf{x}}, \bar{\mu}, E_0, t)$ in gyrocenter coordinates, $Z \equiv (\bar{\mathbf{x}}, \bar{\mu}, E_0, t)$, $\bar{\mathbf{x}} = \mathbf{x} - \rho$, $\rho = \mathbf{b} \times \mathbf{v}/\Omega_{\mathbf{c}\alpha}$, evolves in electrostatic approximation as

$$\frac{\partial F_\alpha}{\partial t} + \bar{\mathbf{v}}_d \cdot \frac{\partial F_\alpha}{\partial \bar{\mathbf{x}}_\perp} + (\bar{v}_{\parallel\alpha} + \bar{v}_{\mathrm{Banos}})\mathbf{b} \cdot \frac{\partial F_\alpha}{\partial \bar{\mathbf{x}}} + \left[q\frac{\partial \langle \Phi_0 \rangle}{\partial t} + \bar{\mu}\frac{\partial B}{\partial t} - \frac{B}{B_\parallel^*}\bar{v}_\parallel q \frac{\partial \langle \delta\phi \rangle}{\partial s} - \mathbf{v}_{d0} \cdot (q\bar{\nabla}\langle \delta\phi \rangle) \right] \frac{\partial F_\alpha}{\partial E_0} = C(F_\alpha, F_\alpha), \quad (1)$$

$$\bar{\mathbf{v}}_d = \frac{c\mathbf{b}}{qB_\parallel^*} \times (q\bar{\nabla}\langle \Phi \rangle + \bar{\mu}\bar{\nabla}B) + \bar{v}_\parallel^2 \frac{M_\alpha c}{qB_\parallel^*}(\bar{\nabla} \times \mathbf{b}), \quad (2)$$

$$\bar{\mathbf{v}}_{d0} = \frac{c\mathbf{b}}{qB_\parallel^*} \times (q\bar{\nabla}\langle \Phi_0 \rangle + \bar{\mu}\bar{\nabla}B) + \bar{v}_\parallel^2 \frac{M_\alpha c}{qB_\parallel^*}(\bar{\nabla} \times \mathbf{b}), \quad (3)$$

$$\bar{v}_\parallel = \pm \sqrt{\frac{2}{M_\alpha}(E_0 - \bar{\mu}B - q\langle \Phi_0 \rangle)}, \quad v_{\mathrm{Banos}} = \frac{\mu c}{q}(\mathbf{b} \cdot \bar{\nabla} \times \mathbf{b}), \quad (4)$$

$$B_{\parallel\alpha}^* \equiv B\left[1 + \frac{\mathbf{b}}{\Omega_{c\alpha}} \cdot (v_\parallel \bar{\nabla} \times \mathbf{b}) \right], \quad \Omega_{c\alpha} = \frac{qB}{M_\alpha c}, \quad \mu = \frac{M_\alpha v_\perp^2}{2B}, \quad (5)$$

$$\langle \delta\phi \rangle = \langle \Phi \rangle - \langle \Phi_0 \rangle. \quad (6)$$

Here, $Z_\alpha e$ and M_α are the electric charges and masses of electrons ($\alpha = e$) and ions ($\alpha = i$). $\bar{\mu}$ is the magnetic moment. The left-hand side of Eq. (1) describes the particle motion in the electric field and magnetic field. C represents the Coulomb collision operator. v_{Banos} is the Banos drift [15]. The overbar is used for the gyrocenter variables and $\langle \cdots \rangle$ denotes the gyroangle averaging. The field Φ is separated into two parts: Φ_0 has large amplitude and slow variation; $\delta\phi$ is small in amplitude and has rapid variation. E_0 is the total energy absent the perturbed potential energy ("almost energy").

In the long wavelength limit $k_\perp \rho_\alpha \ll 1$, the self-consistent electric field is computed from the full-f gyrokinetic Poisson equation for multiple species [14,16,17]

$$\sum_\alpha \frac{\rho_\alpha^2}{2\lambda_{D\alpha}^2} \nabla_\perp \cdot (\ln N_\alpha \nabla_\perp \Phi) + \nabla^2 \Phi = -4\pi e \left[\sum_\alpha Z_\alpha N_\alpha(\mathbf{x}, t) - n_e(\mathbf{x}, t) \right] - \sum_\alpha \frac{\rho_\alpha^2}{4\lambda_{D\alpha}^2} \frac{1}{N_\alpha Z_\alpha e} \nabla_\perp^2 p_{\perp\alpha}. \quad (7)$$

where two additional assumptions are used in the simplification from the general gyrokinetic Poisson equation [12]: (1) Inhomogeneities in ϕ dominate those in the gyrokinetic moments in evaluating the ion polarization density; (2) the perpendicular distribution function is Maxwellian in evaluating the higher-order terms in the gyrokinetic moments. Here n_α and $T_{\perp\alpha}$ are the ion density and temperature, respectively. The ion gyroradius is $\rho_\alpha = v_{T\alpha}/\Omega_\alpha$, where the ion thermal velocity is $v_{T\alpha} = \sqrt{2T_{\perp\alpha}/M_\alpha}$, the ion gyrofrequency is $\Omega_\alpha = Z_\alpha eB/M_\alpha c$, and the ion Debye length is $\lambda_{D\alpha}^2 = T_{\perp\alpha}/4\pi n_\alpha Z_\alpha^2 e^2$. Our gyrokinetic Poisson equation is fully nonlinear with the gyrocenter density N_α and perpendicular ion pressure $p_{\perp\alpha}$, calculated from the gyrocenter distribution function $F_\alpha(\bar{\mathbf{x}}, \bar{\mu}, \bar{E}_0, t)$. The last term of Eq. (7) is the diamagnetic density from the long wavelength expansion of the gyroaveraged gyrocenter density $N_\alpha(\mathbf{x}, t)$ (i.e., from the pullback transform). Although the diamagnetic density is small compared to the ion gyrocenter density, it is of the same order as both the polarization density in high-β plasmas and the difference between the ion and electron gyrocenter densities. This equation is an extension of the typical neoclassical electric field model including poloidal variation.

III. NUMERICAL SCHEMES

We report applications of TEMPEST, a full-f initial-value gyrokinetic code, to simulate neoclassical transport and geodesic-acoustic mode (GAM) relaxation in edge plasmas. This five-dimensional $(\psi, \theta, \zeta, E_0, \mu)$ continuum code represents velocity space via a grid in equilibrium energy (E_0) and magnetic moment (μ) variables, and configuration space via a grid in poloidal magnetic flux (ψ), poloidal angle (θ), and toroidal angle (ζ). The geometry can be a circular annulus or that of a diverted tokamak and includes boundary conditions for both closed magnetic flux surfaces and open field lines. The same set of gyrokinetic equations is discretized for both geometries. The description of the TEMPEST equations, numerical scheme, and verification tests have been given in Ref. [14]. Since this work will focus on the neoclassical simulations of a tokamak plasma in the absence of turbulence, for rapid parameter scans a four-dimensional (4D) (ψ, θ, E_0, μ) TEMPEST running option will be used for a neoclassical transport without an electric field first to benchmark with available theory and then for the development of the neoclassical electric field.

In an axisymmetric configuration, the equilibrium magnetic field is written as $\mathbf{B} = I\nabla\zeta + \nabla\zeta \times \nabla\psi$ where $I = RB_t$. Because the magnetic field is inversely proportional to the major radius $(B \propto 1/R)$, for a given energy E_0 and magnetic moment μ, there are inaccessible regions for particles where $v_\parallel^2 = (2/M_\alpha)(E_0 - \mu B - q\Phi_0) \leq 0$, as indicated on the left-hand side of the annulus with a black (bluish-violet) color in Fig. 1. The crosses are TEMPEST radial and poloidal meshes of the annulus in a tokamak geometry with a circular cross section. The contours of the distribution function $F_0(\psi, \theta, E_0, \mu)$ in gray (orange) represent regions occupied by trapped particles for a given energy E_0 and magnetic moment μ. As the trapped particles move radially outward, the orbit size increases with minor radius, indicated by the green curves in Fig. 1. Therefore, there exist internal boundaries for trapped particles in the radial direction. The straightforward upwinding difference yields instabilities near the internal boundary points. Therefore a fifth-order Weno scheme [18] is routinely used for particle radial drifts.

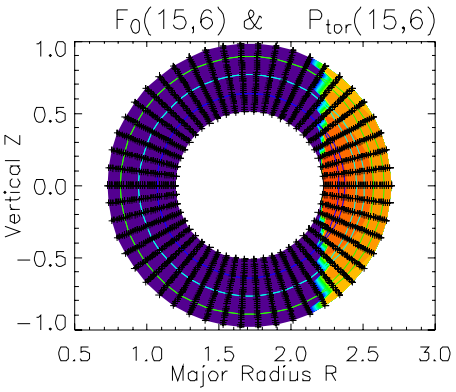

FIG. 1. (Color online) TEMPEST radial and poloidal meshes of an annulus in a tokamak geometry with a circular cross section, indicated by the cross. The contours of the distribution function $F_0(\psi, \theta, E_0, \mu)$ with $E_0 = 15$ and $\mu = 6$ in gray (orange) represent regions occupied by trapped particles for a given energy E_0 and magnetic moment μ, and is overlaid by trapped particle orbits which are the contour plots of canonical toroidal angular momentum $P_{\text{tor}}(\psi, \theta, E_0, \mu) = (q/c)\psi \pm (I/B)M_\alpha v_\parallel$.

There are three constants of motion in an axisymmetric configuration: The total energy $E = M_\alpha v_\parallel^2/2 + \mu B + q\Phi$, the magnetic moment $\mu = M_\alpha v_\perp^2/2B$ [19], and the canonical angular momentum $P_\zeta = (q/c)\psi \pm (I/B)M_\alpha v_\parallel$. The advantage of choosing (E_0, μ) coordinates is that (E_0, μ) remain constant along particle orbits (in the absence of collisions and turbulence $\delta\phi$); this prevents orbit mixing by numerical differencing, and the dynamics associated with particle orbits can be accurately simulated. The disadvantage is in association of the cut cells at the bottom of E_0 and top μ-boundary meshes as shown in Fig. 2(a), where the boundary $v_\parallel^2 = (2/M_\alpha)(E_0 - \mu B - q\Phi_0) = 0$ is a straight line cutting through the background grid and separates the physical (above, $v_\parallel^2 > 0$) and nonphysical (below, $v_\parallel^2 < 0$) zones. The dotted line with $E_0 = \mu B(\psi, \theta)$ when $\Phi_0 = 0$ inside the physical zone $(v_\parallel^2 > 0)$ separates the circulating and trapped particles, where the $B(\psi, \theta)$ is the local magnetic field. Obviously, the advantage in using (E_0, μ) velocity coordinates is that this physical boundary is not a numerical boundary in velocity space (although it is in real space at turning points where $v_\parallel = 0$), and therefore, there is no additional boundary condition for a numerical finite difference across this boundary. The real numerical boundary conditions are as follows. (1) There is no flow out of the μ boundary at $\mu = 0$ and $E_0 = 0$. (2) The two sheets of distribution are continuous at $E_0 = E_{0\,\min}$ and $\mu = \mu_{\max}$ as shown in Fig. 2(b), where $v_{\parallel\alpha} = 0$. Here the two sheets of the distribution refer to the distribution with the sign of velocity: f^+ for $v_\parallel \geq 0$ and f^- for $v_\parallel < 0$ for any given energy E_0 and magnetic moment μ. At the top of the μ mesh, the mesh size for a cut cell is $\Delta\mu_{iv,jv} = 2d\mu$, where $d\mu$ is the distance between the $\mu_{\max} = (E_0 - q\langle\Phi_0\rangle)/B$ at $v_\parallel = 0$ and the maximum μ-boundary grid point before reaching the $\mu_{\max}$ at

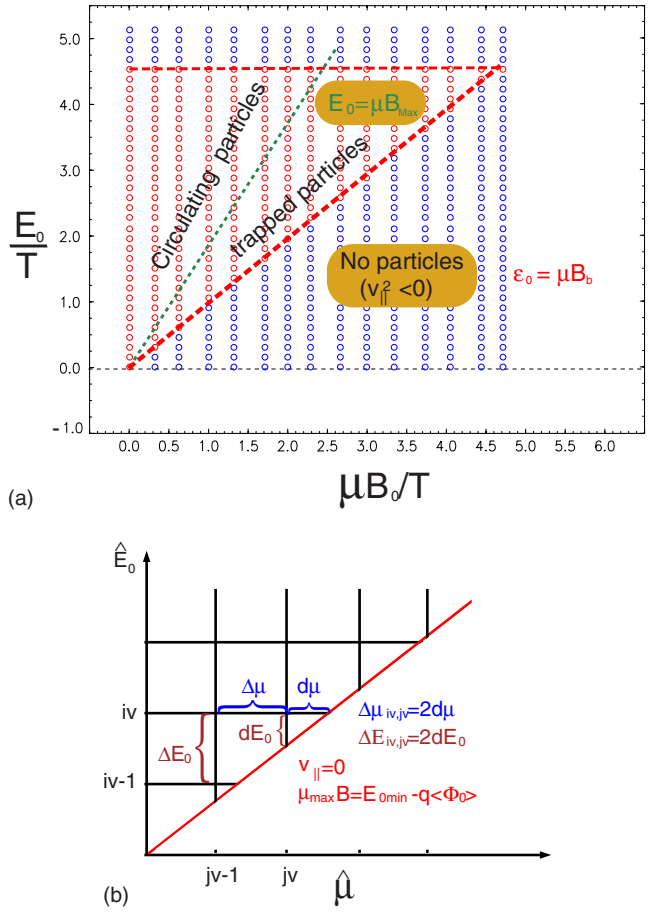

FIG. 2. (Color online) (a) TEMPEST energy E_0 and magnetic moment μ meshes. The boundary $v_\parallel^2=(2/M_\alpha)(E_0-\mu B-q\Phi_0)=0$ is a straight dashed line cutting through the background grid and separating the physical (above, $v_\parallel^2>0$) and nonphysical (below, $v_\parallel^2<0$) zones. (b) A sketch of cut cells at bottom of the energy E_0 and top of the magnetic moment meshes $\mu_{\max}$: $d\mu$ and dE_0.

$v_\parallel=0$ as shown in Fig. 2(b), and where the factor of 2 comes from the equal distance $d\mu$ to the $\mu_{\max}$ for the two sheets of the distribution function. At the bottom of the E_0 mesh, the mesh size for a cut cell is $\Delta E_{0iv,jv}=2dE_0$, where dE_0 is the distance between the $E_{0\,\min}=(\mu_{\max}B+q\langle\Phi_0\rangle)$ at $v_\parallel=0$ and the minimum E_0-boundary grid point above the $E_{0\,\min}$ at $v_\parallel=0$ as shown in Fig. 2(b). The cut cells dE_0 and $d\mu$ will have to be merged with the neighboring regular cells if they are too close to the $v_\parallel=0$ line to avoid arbitrarily small cut cells, which can potentially lead to code blowup. The detailed two-dimensional (2D) description of the cell-cut and merging scheme is given in Ref. [20]. (3) At the top of the energy mesh $E_{0\,\max}$ exponential extrapolation of the distribution F_α in energy is used, assuming $F_\alpha=F_\alpha(E_{0\,\max})\exp[-(E_0-E_{0\,\max})/T_i]$ beyond the simulation domain for $E_0>E_{0\,\max}$.

Radial Robin boundary conditions are used for F_α and the potential Φ at the inner core surface $\psi=\psi_c$ and the outer wall surface $\psi=\psi_w$. Robin boundary conditions consist of specification of a linear combination of a field value and its normal derivative at all points of the boundary surface $\psi=\psi_{c,w}$, such as $\alpha_b\Phi^b+\beta_b\partial\Phi^b/\partial\psi$, where α_b,β_b,Φ^b and $\partial\Phi^b/\partial\psi$ are being prescribed. This is a generalization of Dirichlet ($\alpha_b=1$ and $\beta_b=0$) and Neumann ($\alpha_b=0$ and $\beta_b=1$) boundary conditions. Since the gyrokinetic equation has only a first-order radial advection term, only one boundary condition is used and then only where the convection is into the domain. No boundary condition should be imposed for particles convecting out of the domain; therefore, an extrapolation is used at that boundary.

For neoclassical transport problems, the scale length of the potential L_ϕ is determined by the drift orbit size $\rho_{\theta,i}$ and is typically much larger than the gyroradius (ρ_i, $L_\phi\sim\rho_{\theta,i}\gg\rho_i$), Here $\rho_{\theta,i}$ is the ion gyroradius using the poloidal magnetic field. Hence, there is a boundary layer (a gyrosheath) in Eq. (7) associated with small parameter $\rho_\alpha/L_\phi\ll1$. Therefore, the Poisson equation (7) is rarely solved. Instead, a simplified equation for the radial electric field is used [1,2,6] with the assumption that the electrostatic potential is constant on the flux surface. For edge plasmas, the potential has both radial and poloidal variations due to the end loss in the scrape-off layer, and the assumption is clearly violated. In order to efficiently solve Eq. (7), we develop a scheme here to impose the Neumann boundary conditions $E_\psi=-\partial\phi/\partial\psi=$const at both radial boundary surfaces to eliminate the boundary layer effects. However, when the Neumann boundary condition is used for both radial boundaries $\psi=\psi_c$ and $\psi=\psi_w$, the Poisson problem is ill posed. A technique used is to remove the global net charge from the simulation domain to ensure that the Poisson problem is well posed. This constraint is naturally consistent with the plasma quasineutrality condition. The same technique has been used for doubly periodic boundary conditions [14]. As an illustration, here is a simple example. A one-dimensional (1D) Poisson equation on a domain $0\le x\le a$ with Neumann boundary conditions is $\rho_i^2\partial^2\phi/\partial x^2=\sin(2\pi x/a)$ with $\partial\phi/\partial x=0$ at $x=0$ and $x=a$. Here $\rho_i/a\ll1$. The solution to the corresponding equation exists only if there is no net source in the domain; that is, by integration, $\partial\phi/\partial x|^{x=a}-\partial\phi/\partial x|^{x=0}=\int_0^a dx\,\sin(2\pi x/a)=0$. The solution can be obtained by integration as $\phi(x)=(a/2\pi\rho_i)^2[(2\pi x/a)-\sin(2\pi x/a)]+C_0$. There are three noticeable features of the solution. (1) The solution has an undetermined constant C_0. However, the global constant potential has no physical consequence to the gyrokinetic equation. (2) The solution is a linear composition of a general solution and a particular solution. The general solution is a linear function in radial variable due to the gyro-Poisson operator and the particular solution is a periodic function in radial variable determined by the source. (3) The scale length of potential is determined by the scale length of the source a, not by the small scale length ρ_i at the boundary surfaces. But, when the small scale ($\sim\rho_i$) turbulence along with large-scale orbit size $\sim\rho_{\theta,i}\sim10\rho_i$ coexists in the source, the same equation can be solved for multiple spatial scale lengths. These are the properties needed for the neoclassical turbulent transport simulations.

IV. SIMULATION RESULTS

In our 4D TEMPEST neoclassical simulations, we consider a simple axisymmetric tokamak with the magnetic field in a circular geometry, given by $\mathbf{B}=B_\zeta\mathbf{e}_\zeta+B_\theta\mathbf{e}_\theta$, where ζ and θ

are the toroidal and poloidal angles of a torus, respectively. The poloidal angle θ is chosen such that $\theta=0$ corresponds to the outboard midplane of the torus. The inverse aspect ratio $\epsilon=r/R_0$ is not assumed to be small, where r is the minor radius. The major radius is given by $R=R_0(1+\epsilon\cos\theta)$ and toroidal magnetic field $B_\zeta=B_0R_0/R$. The plasma consists of deuterium ions and electrons. For the physics problems studied in this paper, the gyrokinetic Poisson equation (7) has been used without the diamagnetic density term and Φ_0 has been set to zero. The typical resolution is $n_\psi=32$, $n_\theta=64$, $n_{E_0}=25$, and $n_\mu=50$.

A. Neoclassical radial fluxes

Neoclassical transport results from the random scattering of particle orbits by collisions in a toroidal geometry with an inhomogeneous magnetic field. In this section, we demonstrate how TEMPEST simulation results agree very well with neoclassical theory when using the same collision model. The simulations presented here are carried out for a large aspect ratio circular geometry with magnetic field $B_t=7.5T$, $R_0=45.6$ m, the safety factor $q=\epsilon B_\zeta/B_\theta=3$ and $\epsilon=0.1$. The large B_0 and R_0 are used for the global simulations in order to benchmark with analytical theory in the limit $\delta_i/L_p\ll 1$ for local analysis. Here L_p is a characteristic gradient scale length of the plasma profile. The ion guiding center density and temperature profiles are initialized as a hyperbolic tangent (tanh) function of radius centered around the middle of the simulation domain (such as, $N(\psi)=n_0+n_m\tanh[(\psi-\psi_m)/\Delta_n]$, where $\psi_m=(\psi_0+\psi_L)/2$, $\Delta_n=\delta_n\ln[N(\psi_0)/N(\psi_L)](\psi_L-\psi_0))$, and δ_n is a parameter to control the radial scale length. The boundary ion distribution is a fixed Maxwellian with $N_0=N(\psi_0)$, $n_L=N(\psi_L)=0.9N_0$, $T_{i0}=T_i(\psi_0)=3$ keV, and $T_{iL}=T_i(\psi_L)=0.9T_{i0}$ during a simulation. In this simulation $\delta_n=50.5$, a Lorentz collision model is used. Given boundary conditions and initial profiles, the interior plasmas in the simulations should evolve into a neoclassical steady state.

A series of TEMPEST simulations are conducted to investigate the scaling characteristics of the neoclassical transport as a function of ν_{*i} via a density scan with $N_0=(1\times10^{12},5\times10^{12},1\times10^{13},2\times10^{13},5\times10^{13},1\times10^{14},5\times10^{14},1\times10^{15},5\times10^{15},1\times10^{16})$ cm^{-3}. Here ν_{*i} is the effective collision frequency, defined by $\nu_{*i}=\epsilon^{-3/2}\nu_{ii}\sqrt{2}qR_0/v_{Ti}$, ν_{ii} is the ion-ion collision, and the ion thermal velocity is $v_{Ti}=\sqrt{2T_i(\psi_0)/M_i}$. The peaks of both particle and heat fluxes due to the peak radial gradient drives of density and temperature are shown in Fig. 3, along with the analytical predictions of Lin *et al.* [21] using a Lorentz collision operator with a constant frequency. The radial particle and heat flux here and in the rest of the paper imply the corresponding flux-surface-averaged fluxes. A time history of the radial heat flux profile in Fig. 4(a) for $\nu_{*i}=4.5$ in the plateau regime from TEMPEST shows that the simulation reaches steady-state solutions; the same is true for other ν_{*i} simulations in the scan. A good agreement is obtained both in the banana and collisional regimes, where the analytical theories are valid. The differences between Fig. 3 here and Fig. 2 of Ref. [16] are simulation parameters and the Lorentz collision model used, besides the plotting variables (fluxes vs diffusivities). Here a simple constant-ν Lorentz model is used for better comparisons with the same constant-ν theory, while in Ref. [16], an energy-dependent Lorentz collision operator was used. In the plateau regime with $\nu_{*i}=4.5$ as shown in Fig. 4, the peak ion heat flux converges with velocity resolution, 1.1% variation over the following scans: $(n_{E_0}=25,\ n_\mu=50,\ E_{0\,\max}=10T_i)$, $(n_{E_0}=50,\ n_\mu=75,\ E_{0\,\max}=10T_i)$, and $(n_{E_0}=50,\ n_\mu=75,\ E_{0\,\max}=20T_i)$. For all cases, $n_\psi=32$ and $n_\theta=128$. However, no clear neoclassical plateau regime is observed in Fig. 3 for the peak ion heat flux from simulations with these parameters and the detailed investigation will be cast in a future presentation.

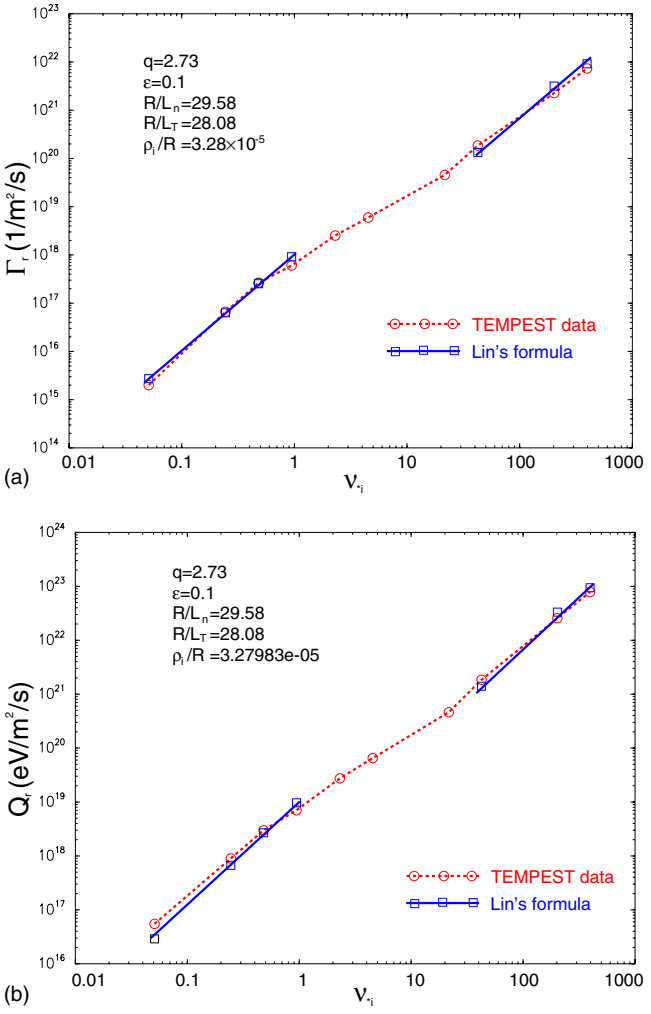

FIG. 3. (Color online) Radial particle Γ_r (a) and heat flux Q_r (b) vs dimensionless collision frequency ν_{*i} from TEMPEST simulation of neoclassical ion transport with $\phi=0$. Here a Lorentz collision operator is used. The solid lines are analytical predictions of Lin *et al.* [21].

An interesting property of the neoclassical radial fluxes is checked in the $\nu_{*i}\ll 1$ regime. Because in this regime collisions are negligibly small, the particle orbits should be almost closed; and therefore there should be almost no net radial fluxes. A time history of the radial heat flux profile is shown in Fig. 4(b) for $\nu_{*i}=0.0006$ with $N_0=1\times10^{10}$ cm^{-3} in the deep banana regime from TEMPEST simulations. The ra-

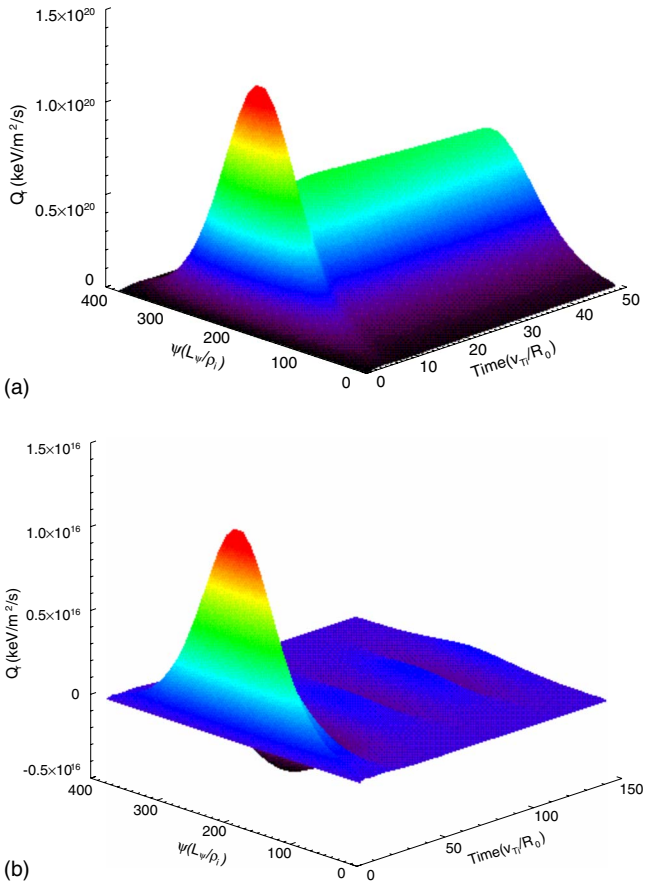

FIG. 4. (Color online) Radial profile of radial heat flux Q_r for (a) $\nu_{*i}=4.5$ and (b) $\nu_{*i}=0.0006$ vs time in the unit of v_{Ti}/R from TEMPEST simulation of neoclassical ion transport with $\phi=0$. Here a Lorentz collision operator is used.

dial heat flux oscillates in time at all radial locations with the same frequency. Figure 5 shows that after an initial adjustment due to the arbitrary initial conditions, the oscillation

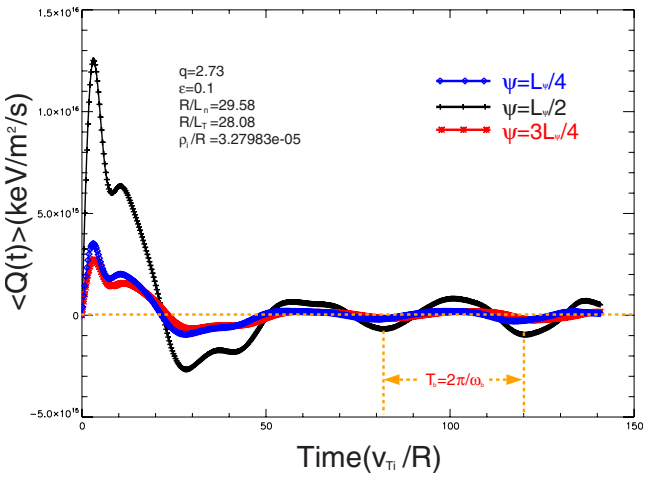

FIG. 5. (Color online) Radial heat flux Q_r vs time in the unit of v_{Ti}/R from TEMPEST simulation of neoclassical ion transport with $\phi=0$ and $\nu_{*i}=0.0006$ as Fig. 4(b) for three different radial positions. Here a Lorentz collision operator is used. L_ψ is the radial box size.

frequency is the thermal trapped particle bounce frequency with $\omega_b=\sqrt{\epsilon/2}(v_{Ti}/qR_0), v_{Ti}=\sqrt{2T_i(\psi_0)/M_i}$. The time-averaged flux is nearly zero during the late time, which is consistent with the physical expectation.

Note that in a truly steady state, the particle and heat fluxes should be radial constants in the absence of the volume sources and sinks; however it is apparently not the case in Fig. 4(a). As we discussed in the last paragraph of the introduction, a full-f neoclassical simulation involves several types of physics interacting over several scales in time and space: (1) ion orbital dynamics; (2) the neoclassical transport; and (3) a global truly rotational steady state involving the radial boundary conditions. Neoclassical transport is a local transport which depends on the local radial gradient of the profile. During the development of neoclassical transport due to the random scattering of particle orbits by Coulomb collisions in stage (2), the profile has not been changed appreciably from the initial one. Because of the scale separation, we see a relatively steady state for the fluxes in time, and the fluxes are proportional to the local radial gradient of the profile as the neoclassical theory predicted. This is the stage that is plotted in Fig. 4(a).

B. Radial propagation of geodesic-acoustic modes and relaxation of the neoclassical electric field

The geodesic-acoustic mode (GAM) is a poloidally asymmetric mode with a coherent and radially localized poloidal flow oscillation that is dominant in the outer regions of magnetically confined toroidal plasmas [22,23]. This mode is characterized by oscillations of the plasma column in the vertical direction with a characteristic frequency $\omega_{\mathrm{GAM}} \simeq (\sqrt{7}/2)f(q)(v_{Ti}/R_0)$, where $f(q)=\sqrt{1+46/49q^2}$, and R_0 is the major radius of a torus. The GAM is a normal mode in a homogeneous plasma, involving particle parallel streaming, cross-field drifts, and acceleration.

In this section, we show the development of a neoclassical electric field with Lorentz collisions through different phases and the radial propagation of the GAM at the initial phase in TEMPEST simulations from radially inhomogeneous plasmas. During the relaxation of the electric field after the initial GAM phase and Rosenbluth-Hinton residual zonal flow, the neoclassical radial electric field from the TEMPEST simulations follows the standard neoclassical expression for parallel flow in the plateau regime.

1. Simulation setup

The simulations presented here are carried out for a circular geometry with DIII-D edge parameters: Magnetic field $B_t=1.5T$, $R_0=1.71m$, $q=4$, and $\epsilon=0.3$. The ion guiding-center density and temperature profiles are initialized as a hyperbolic tangent (tanh) function of radius centered around the middle of the simulation domain $(N(\psi)=n_0+n_m\tanh[(\psi-\psi_m)/\Delta_n]$, where $\psi_m=(\psi_w+\psi_c)/2$ and $\Delta_n=\delta_n \ln(N_c/N_w)(\psi_w-\psi_c))$. δ_n is a parameter to control the radial scale length. In this simulation, $\delta_n=50.5$, and a Lorentz collision model is used. The boundary ion distribution is a fixed Maxwellian with $N_c=N(\psi_c)=1\times10^{19}m^{-3}$, $N_w=N(\psi_w)=0.9N_c$, $T_{ic}=T_i(\psi_c)=300$ eV, and $T_{iw}=T_i(\psi_w)$

$=0.9T_{ic}$ during a simulation. The radial boundary condition for the potential is $\partial\phi(\psi_c)/\partial\psi=\partial\phi(\psi_w)/\partial\psi=0$. The electron model is the fully nonlinear Boltzmann model. The Boltzmann model for a closed-flux surface is defined as $n_e=\langle n_i(\psi,\theta,t=0)\rangle\exp(e\phi/T_e)/\langle\exp(e\phi/T_e)\rangle$, where $\langle\cdots\rangle$ represents the flux surface average. The property of the Boltzmann model is $\langle n_e\rangle=\langle n_i(\psi,\theta,t=0)\rangle$, so there is no net radial electron transport. An initial pulselike perturbation of the ion density is given with the peak centered around the middle of the pedestal $\delta n_i=\delta N_0(\psi-\psi_m)e^{-[(\psi-\psi_m)/\Delta_{\delta n}]^2}$, where $dN_0=0.001$ and $\Delta_{\delta n}=0.094(\psi_w-\psi_c)$.

2. Simulation results

A time history of the potential from TEMPEST shows in Fig. 6(a) the GAM generated by the initial conditions, damped by the wave-particle resonances and then relaxed to a Rosenbluth-Hinton residual zonal flow [24–26]. The TEMPEST simulations correctly calculate the GAM frequency ω_{GAM} and the collisionless damping rate γ_{GAM} in homogeneous plasmas. Extensive studies of wave-particle resonances and benchmarking with theory have been demonstrated in Ref. [27]. Figure 6(b) shows a contour plot of the perturbed ion density as a function of a time and radial position. The linear relationship of ion density contour between time and radial position (line with arrows) indicates that the group velocity and phase velocity are the same. For any given radial location, the GAM oscillates and decays due to the collisionless and collisional damping, as shown in the potential time history in Fig. 6(a).

One of the most striking features is that the density perturbation radially propagates outward inside the pedestal where the temperature is radially inhomogeneous with $v_{p\psi}^{\mathrm{sim}}\simeq 12.05(\rho_s/R)v_{thi}$ for $q=4$, which is qualitatively consistent with experimental measurements [28,29], and also consistent with a kinetic GAM theory [30,31]. In the theory, the GAM is generated by turbulent excitation via three-wave resonant coupling of a kinetic GAM (KGAM), which is the short wavelength counterpart of the usual GAM, due to finite ion Larmor radii and finite magnetic drift orbit widths. The GAM spectrum in a radially nonuniform toroidal plasma is continuous due to the dependence of the frequency on the local temperature $T_i(\psi)$ and/or the safety factor $q(\psi)$ $\{\omega_{\mathrm{GAM}}^2(\psi)\simeq(7/2)f^2[q(\psi)][T_i(\psi)/M_iR_0^2]\}$. The local dispersion relation turns into a radial wave equation in a radially nonuniform plasma with $k_\psi=-i\partial/\partial\psi$ when the finite-ion-Larmor-radius effect is retained $[\omega^2=\omega_{\mathrm{GAM}}^2(\psi)+C(\psi,\omega)k_\psi^2\rho_i^2$, where $C(\psi,\omega)$ is a complicated expression [30–32]]. The resultant radial wave equation with outgoing wave boundary conditions leads to KGAM propagation toward the low-temperature and/or high q domain where $\omega^2>\omega_{\mathrm{GAM}}^2(\psi)$. The linear temperature profile $T_i(\psi)=T_0+T_1(\psi_0-\psi)$ is a simple model for an edge plasma in one spatial dimension. The radial wave equation admits an analytical solution for this temperature profile in terms of the Airy function with outgoing wave boundary conditions [31]. In TEMPEST simulations, the radial propagation velocity $v_{p\psi}$ is found to be weakly dependent on q, and it increases as q decreases, mostly due to the q dependence of the GAM frequency ω_{GAM} for the fixed plasma profiles. In the absence of a kinetic GAM theory which should yield a self-consistent radial mode structure and dispersion relation in an inhomogeneous plasma with outgoing wave boundary conditions,

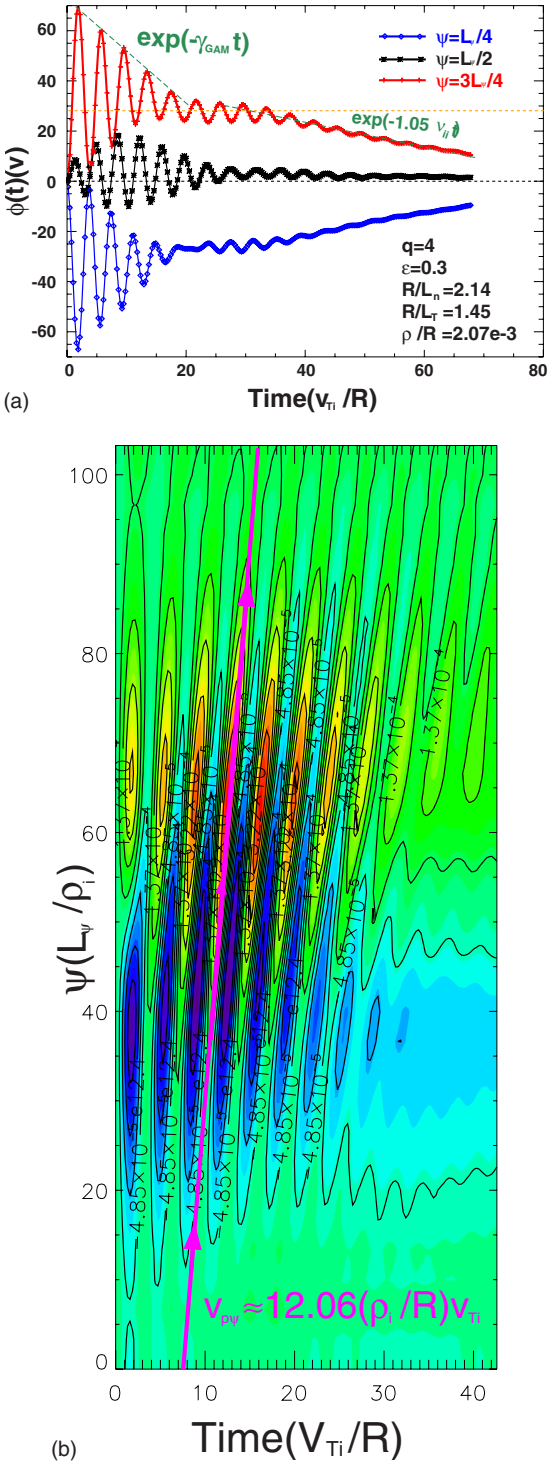

FIG. 6. (Color online) (a) Time evolution of the zonal-GAM potential $\phi(t)$ shows GAM oscillation, collisionless damping, and collisional damping of zonal flow residual for a circular geometry with $q=4$ and $\epsilon=0.3$. $n_\psi=32$, $n_\theta=64$, $n_{E0}=30$, $n_\mu=60$, and $K_{E,\max}=20T_i$; (b) Contour plot of perturbed ion density $\delta n_i/N_{i0}=(N_i-N_{i0})/N_{i0}$ as a function of a radial position and time for the same parameters. Here L_ψ is the radial box size.

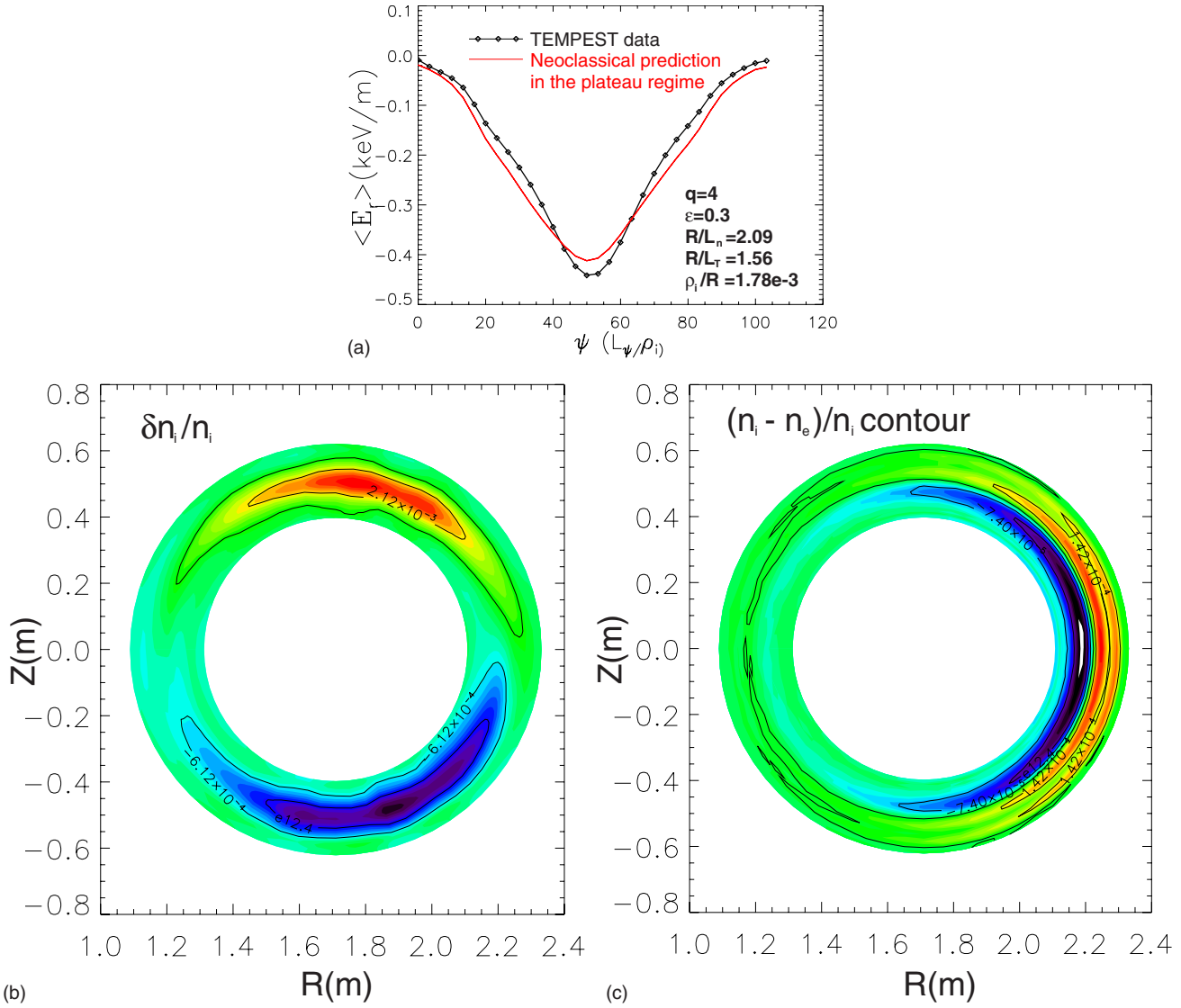

FIG. 7. (Color online) (a) E_ψ from TEMPEST simulations (black) vs neoclassical prediction in the plateau regime, and contours of (b) the relative perturbed ion density $\delta n_i/N_{i0}=(N_i-N_{i0})/N_{i0}$ and (c) the relative charge density $(N_i-N_e)/N_i$ from TEMPEST simulation of neoclassical ion transport during the GAM oscillations.

we estimate the theoretical phase velocity $v_{p\psi}^{th}=\omega_{\mathrm{GAM}}/k_\psi$ based on the characteristic scale length $\lambda_{\mathrm{GAM}}\sim\pi\rho_i(L_{Ti}/\rho_i)^{1/3}$ around the peak gradient position [31], which yields $\lambda_{\mathrm{GAM}}^{th}\sim 22.3546\rho_i$ and $v_{p\psi}^{th}=\omega_{\mathrm{GAM}}/k_\psi=(\sqrt{7}/2)f(L_{Ti}/\rho_i)^{1/3}(\rho_i/R)v_{Ti}=15.9471(\rho_i/R)v_{Ti}$. Comparing with the measured velocity $v_{p\psi}^{\mathrm{sim}}$ in Fig. 6(b), the preliminary estimate of the radial propagation velocity agrees to within 32% accuracy between theory and simulation. The difference is possible due to the following reasons: (1) The local linear expansion of ion temperature profile in the theory for simplicity; (2) an accurate analysis of particle orbit has been ignored which may modify the coefficient $C(\psi,\omega)$ associated with the finite-ion-Larmor-radius effect. In closing it is worthy to note here that by imposing radial Dirichlet boundary conditions on potential $[\phi(x=-\infty)=0$ and $\phi(x=L_{Ti})=0]$ and assuming a linear ion temperature profile in a slab geometry, Ref. [32] shows that the GAM becomes an eigenmode rather than wavelike radial structure, and the GAM has discrete eigenfrequency, rather than having a continuous spectrum. However, the dispersion relation given by Eq. (1) of Ref. [32] does not reduce to the known solutions in Refs. [25–27,30]; especially the coefficient of the finite gyoradius effect $C=0$ when $T_e=0$ in Ref. [32], which disagrees with the results in Refs. [30,31].

3. Neoclassical polarization

Due to the existence of ion-ion collisions, the Rosenbluth-Hinton residual is damped with a damping rate $\propto\nu_{ii}$ as shown in Fig. 6(a), and then the potential approaches the neoclassical residual. The collisional damping rate as measured is $\gamma_c\simeq 1.05\nu_{ii}$, which is smaller than local calculations with the $\epsilon\ll 1$ approximation: $\gamma_{HR}=\nu_{ii}/(0.64\sqrt{\epsilon})\simeq 2.852\,72\nu_{ii}$ [33] and $\gamma_{XC}=\nu_{ii}/(4\epsilon^{3/2})\simeq 1.52145\nu_{ii}$ [34]. During the development of the electric field after the initial GAM phase, the neoclassical radial electric field from TEMPEST simulations is shown in Fig. 7(a), along with the standard neoclassical re-

lationship between the radial electric field and the parallel flow $\langle U_{i\|}\rangle=(cT_i/Z_ieB_p)[k(\partial \ln T_i/\partial r)-(\partial \ln P_i/\partial r)-(Z_ie/T_i)(\partial\langle\Phi\rangle/\partial r)]$ with k=−0.5 in the plateau regime [35]. The radial electric field $E_\psi=-\partial\langle\Phi\rangle/\partial\psi$ is calculated from the solution of gyrokinetic Poisson equation and the ion temperature T_i, pressure P_i and parallel velocity $U_{i\|}$ are obtained from the moments of gyrokinetic distribution function. It is found that the magnitude of the parallel velocity is much smaller than the ion thermal velocity and the effective $\mathbf{E}\times\mathbf{B}$ velocity. The radial electric field is generated from the neoclassical polarization [24]: The spreading of the charge cloud for the trapped ions over the thickness of their banana orbits due to the toroidal magnetic geometry. Figures 7(b) and 7(c) show the contours of the relative ion density perturbation and the relative charge density from the TEMPEST simulation. Due to the orbital dynamics inside the magnetic well as shown in Fig. 1, a particle at the outside midplane streams up and drifts outward from high density to low density on the upper half of the plane, then bounces back from the upper turning point, streams down and drifts inward from low density to high density in the lower one-half of the plane, bounces back from a lower turning point, and repeats the process again and again. The combination of the particle orbits and the radial profile of the density yields poloidal as well as radial variation of ion density. Because of the large ion to electron mass ratio, the resulting difference in orbit size creates a neoclassical polarization—a poloidal and radial variation of the charge density spreading over the thickness of ion banana orbits, as shown in Fig. 7(c) which can be compared with banana orbits in Fig. 1. However, the poloidal variation of the potential is nevertheless small in circular geometry.

C. Steady-state neoclassical electric field and ambipolarity of neoclassical transport

The simulations presented here are carried out with the same model and parameters as in Sec. IV B, except in this section $q=2$, $\nu_{*i}=2.1$, and the ion temperature profile is flat. Figure 8(a) shows the time evolution of the electric potential at $\psi=0.25L_\psi$, $\psi=0.5L_\psi$, and $\psi=0.75L_\psi$. The time unit corresponds to one GAM time (v_{Ti}/R_0). The electrostatic potential relaxes to a steady state, with the GAM in the initial phase damped by Landau resonance and ion-ion collisions. Figure 8(b) shows the steady-state radial profiles of potential $\phi(\psi)$ (red curve with diamond) and density $-\ln[N_i(\psi)/N_i(\psi=0.5L_\psi)]$ (black) from TEMPEST simulations. Here L_ψ is the radial box size. A Boltzmann relation is reached for the steady-state potential, $(Z_ie/T_i)\partial\phi/\partial\psi+\partial \ln P_i/\partial\psi=0$, as expected from the theory for the case of zero temperature gradient [36]. The potential is a superposition of a linear function in the radial variable due to the gyro-Poisson operator (the classical ion polarization) and a periodic function due to the neoclassical polarization, as discussed in the last paragraph of Sec. III. The small differences between the red with diamond and black curves in Fig. 8(b) are about 5.8% at $\psi=30.4$ and 7.4% at $\psi=70.9$, and are possibly due to the contribution from the classical ion polarization. The steady-state parallel velocity is very small due to the specified Maxwellian radial boundary condition with zero flow velocity. The ambipolarity of neoclassical transport with a self-consistent electric field is numerically demonstrated in Fig. 9(a) and compared to the case without E_ψ in Fig. 3(a). With no electric field, a considerable self-collision driven ion flux is found and violates ambipolarity [6]. By choosing the Boltzmann electron model, the radial neoclassical electron flux is zero; the quasineutrality constraint forces the net flux-surface-averaged radial ion flux to be zero through the self-consistent radial electric field and its gradient producing orbit squeezing and expansion due to finite-orbit-width effect, which is consistent with the PIC δf simulations [6]. The tiny residual flux in Fig. 9(a) is possibly due to the nonconserving Lorentz collision model used and/or the small poloidal varying potential [8,37]. Since there is no temperature gradient, the initial GAM exists in the form of a radial eigenmode as a stationary wave without radial propagation as shown in Fig. 9(b) and compared to the case with a temperature gradient in Fig. 6(b). This confirms that the ion temperature inhomoge-

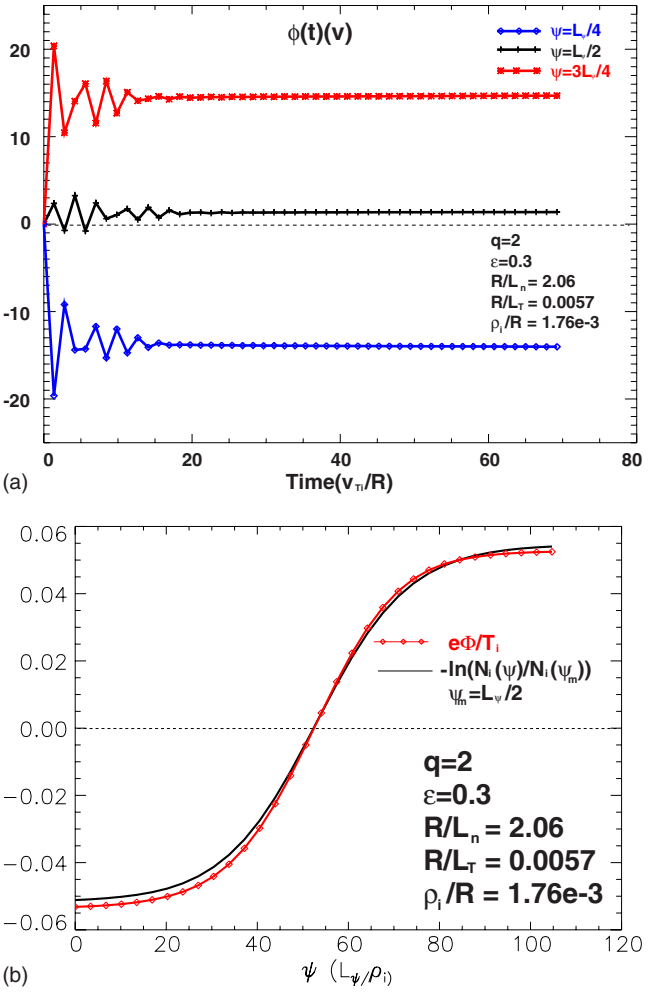

FIG. 8. (Color online) In circular geometry with DIII-D parameters as in Fig. 7 in the plateau regime, except $q=2$ and flat ion temperature profile: (a) Time evolution of electrostatic potential $\phi(t)$ from TEMPEST simulations at $\psi=0.25L_\psi$, $\psi=0.5L_\psi$, and $\psi=0.75L_\psi$, (b) Steady-state radial profiles of potential $\phi(\psi)$ (red with diamond) and density $-\ln[N_i(\psi)/N_i(\psi=0.5L_\psi)]$ (black) from TEMPEST simulations, obeying a Boltzmann relation.

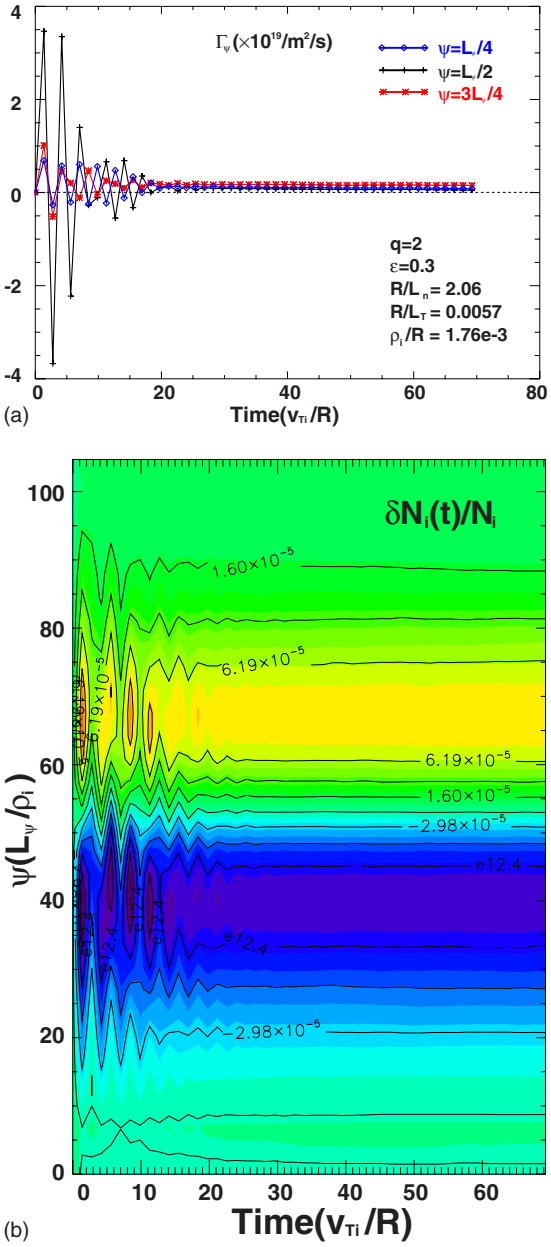

FIG. 9. (Color online) In circular geometry with DIII-D parameters as in Fig. 7 in the plateau regime, except $q=2$ and flat ion temperature profile: (a) Time evolution of a radial ion particle flux $\Gamma_\psi(t)$ from TEMPEST simulations at $\psi=0.25L_\psi$, $\psi=0.5L_\psi$, and $\psi=0.75L_\psi$. The local ion flux evolves to a zero steady-state value when the self-consistent electric field is generated. (b) Contour plot of perturbed ion density $\delta n_i/N_{i0}=(N_i-N_{i0})/N_{i0}$ as function of radial position and time for the same parameters.

neity is a key factor for GAM radial propagation.

V. DISCUSSIONS AND SUMMARIES

We present gyrokinetic neoclassical simulations of tokamak plasmas with a self-consistent electric field for the first time using a full-f continuum code TEMPEST in a circular geometry. We verified the numerical simulation results with a standard neoclassical theory, using the 4D version of the TEMPEST code with Lorentz collisions. In a very-low collisionality regime, an oscillatory flux in time has been demonstrated, as one might expect, because the particles almost stay on closed orbits.

A numerical technique is presented to efficiently solve the gyrokinetic Poisson equation with double Neumann radial boundary conditions for neoclassical simulations. The simulation results are found to agree very well with the classical theory for the development of a neoclassical electric field with Lorentz collisions in the plateau regime. In the initial phase of the development of the neoclassical electric field, we found that ion temperature inhomogeneity is a key factor for GAM radial propagation. The density and radial electric field perturbation radially propagates outward only inside the pedestal where the temperature is inhomogeneous. Otherwise the GAM exists in the form of a radial eigenmode as a stationary wave without radial propagation. During the development of the electric field after the initial GAM phase, the neoclassical radial electric field from TEMPEST simulations follows the standard neoclassical relationship between the radial electric field and the parallel flow in the plateau regime. In steady state, the Boltzmann relation is reached between the electrostatic potential and the ion density for the case of zero temperature gradient, and the quasineutrality constraint forcing the net radial ion flux to be zero is numerically demonstrated.

ACKNOWLEDGMENTS

This work was performed under the auspices of the U.S. Department of Energy by Lawrence Livermore National Laboratory in part under Contract No. W-7405-Eng-48 and in part under Contract No. DE-AC52-07NA27344. We thank Dr. M. R. Dorr, Dr. J. A. Hittinger, and Dr. P. Colella for the math-code infrastructure and software support, and Dr. E. Belli, Dr. J. Candy, Dr. L. Chen, Dr. B. I. Cohen, Dr. R. H. Cohen, Dr. Z. Gao, Dr. R. D. Hazeltine, Dr. F. L. Hinton, Dr. G. D. Kerbel, Dr. W. M. Nevins, Dr. S. Krasheninnikov, Dr. H. Qin, Dr. T. D. Rognlien, Dr. P. B. Snyder, Dr. M. V. Umansky, Dr. W. X. Wang, Dr. Y. Xiao, and Dr. Z. Xiong for fruitful physics discussions. In addition, we wish to acknowledge Dr. R. H. Cohen, Dr. G. D. Kerbel, and Dr. Z. Xiong for contributions to the TEMPEST coding, Dr. B. I. Cohen, and Dr. R. H. Cohen for reading the manuscript.

APPENDIX: RADIAL AMPÉRE-MAXWELL LAW

The Ampére-Maxwell law can be written in differential form

$$4\pi\mathbf{J}+\frac{\partial\mathbf{E}}{\partial t}=c\nabla\times\mathbf{B}. \tag{A1}$$

The radial component of Ampére-Maxwell law can then be written in the form

$$4\pi(\mathbf{J}\cdot\nabla\psi)+\frac{\partial(\mathbf{E}\cdot\nabla\psi)}{\partial t}=c\nabla\times\mathbf{B}\cdot\nabla\psi=c\nabla\cdot(\mathbf{B}\times\nabla\psi). \tag{A2}$$

where the mathematic property $\nabla \times \nabla \psi = 0$ is used. Therefore, the radial component of Ampére-Maxwell law averaged over a closed-flux surface becomes

$$4\pi \langle \mathbf{J} \cdot \nabla \psi \rangle + \frac{\partial \langle \mathbf{E} \cdot \nabla \psi \rangle}{\partial t} = c \langle \nabla \cdot (\mathbf{B} \times \nabla \psi) \rangle = 0. \quad \text{(A3)}$$

[1] J. A. Heikkinen *et al.*, J. Comput. Phys. **173**, 527 (2001).
[2] C. S. Chang, S. Ku, and H. Weitzner, Phys. Plasmas **11**, 2649 (2004).
[3] A. B. Langdon, Phys. Fluids **22**, 163 (1979).
[4] C. K. Birdsall and A. B. Langdon, *Plasma Physics via Computer Simulation* (McGraw-Hill, New York, 1985).
[5] W. M. Nevins and G. W. Hammett (private communication).
[6] W. X. Wang, F. L. Hinton, and S. K. Wong, Phys. Rev. Lett. **87**, 055002 (2001);W. X. Wang *et al.*, Phys. Plasmas **13**, 082501 (2006);
[7] S. Ku *et al.*, J. Phys. **46**, 87 (2006).
[8] E. Belli (private communication).
[9] R. G. Littlejohn, Phys. Fluids **24**, 1730 (1981).
[10] D. H. E. Dubin, J. A. Krommes, C. Oberman, and W. W. Lee, Phys. Fluids **26**, 3524 (1983).
[11] A. J. Brizard and T. S. Hahm, Rev. Mod. Phys. **79**, 421 (2007).
[12] H. Qin, R. H. Cohen, W. M. Nevins, and X. Q. Xu, Contrib. Plasma Phys. **46**, 477 (2006); H. Qin, R. H. Cohen, W. M. Nevins, and X. Q. Xu, Phys. Plasmas **14**, 056110 (2007).
[13] T. S. Hahm, Phys. Plasmas **3**, 4658 (1996).
[14] X. Q. Xu, Z. Xiong, M. R. Dorr, J. A. Hittinger, K. Bodi, J. Candy, B. I. Cohen, R. H. Cohen, P. Colella, G. D. Kerbel, S. Krasheninnikov, W. M. Nevins, H. Qin, T. D. Rognlien, P. B. Snyder, and M. V. Umansky, Nucl. Fusion **47**, 809 (2007).
[15] A. Banos, J. Plasma Phys. **1**, 305 (1967).
[16] R. H. Cohen and X. Q. Xu, Contrib. Plasma Phys. **48**, 212 (2008).
[17] W. W. Lee, J. Comput. Phys. **72**, 243 (1987).
[18] G. S. Jiang and C. W. Shu, J. Comput. Phys. **126**, 202 (1996).
[19] Strictly speaking, the magnetic moment μ is only an adiabatic invariant, but is taken as a true constant of motion up to the first order of gyrokinetic ordering.
[20] Z. Xiong, R. H. Cohen, T. D. Rognlien, and X. Q. Xu, J. Comput. Phys. **227**, 7192 (2008)
[21] Z. Lin, W. M. Tang, and W. W. Lee, Phys. Plasmas **2**, 2975 (1995).
[22] N. Winsor, J. L. Johnson, and J. M. Dawson, Phys. Fluids **11**, 2448 (1968).
[23] K. Hallatschek and D. Biskamp, Phys. Rev. Lett. **86**, 1223 (2001).
[24] M. N. Rosenbluth and F. L. Hinton, Phys. Rev. Lett. **80**, 724 (1998).
[25] H. Sugama and T.-H. Watanabe, Phys. Rev. Lett. **94**, 115001 (2005).
[26] H. Sugama and T.-H. Watanabe, J. Plasma Phys. **72**, 825 (2006).
[27] X. Q. Xu, Z. Xiong, Z. Gao, W. M. Nevins, and G. R. McKee, Phys. Rev. Lett. **100**, 215001 (2008).
[28] T. Ido *et al.*, Plasma Phys. Controlled Fusion **48**, S41 (2006).
[29] T. Lan *et al.*, Phys. Plasmas **15**, 056105 (2008).
[30] F. Zonca and L. Chen, EPL **83**, 35001 (2008).
[31] K. Itoh *et al.*, J. Plasma Fusion Res. **1**, 037 (2006).
[32] M. Sasaki, K. Itoh, A. EJiri, and Y. Takase, Contrib. Plasma Phys. **48**, 68 (2008).
[33] F. L. Hinton and M. N. Rosenbluth, Plasma Phys. Controlled Fusion **41**, A653 (1999).
[34] Y. Xiao and P. J. Catto, Phys. Plasmas **14**, 055910 (2007).
[35] F. L. Hinton and R. D. Hazeltine, Rev. Mod. Phys. **48**, 239 (1976).
[36] M. N. Rosenbluth, P. H. Rutherford, J. B. Taylor, E. A. Frieman, and L. M. Kovrizhnikh, *Plasma Physics and Controlled Nuclear Fusion Research, 1970* (International Atomic Energy Agency, Vienna, 1971), Vol. 1, p. 495.
[37] F. L. Hinton and M. N. Rosenbluth, Phys. Fluids **16**, 836 (1973).